OPEN ACCESS
IOP Publishing
Journal of Physics: Condensed Matter
J. Phys.: Condens. Matter **34** (2022) 465701 (12pp)
https://doi.org/10.1088/1361-648X/ac926a

Role of vibrational properties and electron–phonon coupling on thermal transport across metal-dielectric interfaces with ultrathin metallic interlayers

Shany Mary Oommen[1], Lorenzo Fallarino[2,5], J Heinze[3], Olav Hellwig[2,3] and Simone Pisana[1,4,*]

[1] Department of Physics and Astronomy, York University, Toronto, Canada
[2] Institute of Ion Beam Physics and Materials Research, Helmholtz-Zentrum Dresden-Rossendorf, Dresden, Germany
[3] Institute of Physics, Chemnitz University of Technology, Chemnitz, Germany
[4] Department of Electrical Engineering and Computer Science, York University, Toronto, Canada

E-mail: pisana@yorku.ca

Received 17 May 2022, revised 7 September 2022
Accepted for publication 15 September 2022
Published 23 September 2022

Abstract

We systematically analyze the influence of 5 nm thick metal interlayers inserted at the interface of several sets of different metal-dielectric systems to determine the parameters that most influence interface transport. Our results show that despite the similar Debye temperatures of Al_2O_3 and AlN substrates, the thermal boundary conductance measured for the Au/Al_2O_3 system with Ni and Cr interlayers is $\sim 2\times$ and $>3\times$ higher than the corresponding Au/AlN system, respectively. We also show that for crystalline SiO_2 (quartz) and Al_2O_3 substrates having highly dissimilar Debye temperature, the measured thermal boundary conductance between Al/Al_2O_3 and Al/SiO_2 are similar in the presence of Ni and Cr interlayers. We suggest that comparing the maximum phonon frequency of the acoustic branches is a better parameter than the Debye temperature to predict the change in the thermal boundary conductance. We show that the electron–phonon coupling of the metallic interlayers also alters the heat transport pathways in a metal-dielectric system in a nontrivial way. Typically, interlayers with large electron–phonon coupling strength can increase the thermal boundary conductance by dragging electrons and phonons into equilibrium quickly. However, our results show that a Ta interlayer, having a high electron–phonon coupling, shows a low thermal boundary conductance due to the poor phonon frequency overlap with the top Al layer. Our experimental work can be interpreted in the context of diffuse mismatch theory and can guide the selection of materials for thermal interface engineering.

[5] Now at CIC energiGUNE, Vitoria - Gasteiz, Basque Country, Spain.
[*] Author to whom any correspondence should be addressed.

Supplementary material for this article is available online

Keywords: thermal boundary conductance, metal-dielectric interfaces, Debye temperature, phonon frequencies, time-domain thermoreflectance

(Some figures may appear in colour only in the online journal)

1. Introduction

The control of heat transport at solid–solid interfaces is critical in several energy conversion and heat management applications such as thermoelectrics, microelectronics, photonic and plasmonic devices [1–4]. Various interfacial heat transport mechanisms provide numerous ways to tune the heat transport, hence, understanding the contributions from each will lead to engineering novel micro and nano-electronic devices with optimal thermal performance. It is often possible to tune the heat transport at interfaces by inserting a thin additional layer having specific thermophysical properties, where it is generally accepted that the interlayer should bridge the vibrational properties of the adjacent materials to increase the interface conductance. Typically, layers of intermediate Debye temperatures are chosen, whereas the electron–phonon coupling (EPC) is less often considered as a dominant factor. However, these mechanisms are not well understood particularly for ultrathin interlayers, and the general approach of using materials with intermediate Debye temperatures can fail.

Interfacial thermal transport is quantified by the thermal boundary conductance $G = q/\Delta T$, where q is the heat flux across the boundary and ΔT is the temperature difference. G can be modified (enhanced or reduced) by tuning the various factors affecting interfacial heat transport, such as, for the case of metal-dielectric interfaces, microstructural characteristics of the interface such as roughness, electron–phonon interaction, and phonon–phonon interaction [5–10]. For example, Duda and Hopkins [11] demonstrated that G can be reduced by introducing roughness at the interface, due to increased phonon scattering. Enhancing the interfacial bonding between metal and dielectric has also been found to significantly improve G due to the improved phonon transmission across the interface [12, 13]. Previous works have also shown that the insertion of a thin metallic interlayer can significantly alter G at a metal-dielectric interface by providing a material that can bridge mismatched phonon modes [14–21]. Cheaito *et al* [17] analyzed G across a range of metal/native-oxide/Si and metal/Al_2O_3 systems, showing that the phonon spectral contribution to G depends on the cut-off frequencies of the materials comprising the interface. Jeong *et al* [14] showed that the insertion of a thin metal layer between a metal and dielectric with an intermediate Debye temperature could significantly increase G. They reported enhancements of ∼80% and ∼60% by inserting Cr and Cu interlayers at the Au/Al_2O_3 interface, respectively. Chen *et al* [18] analytically showed that inserting interlayers with strong EPC constant between Au/Al_2O_3 can reduce the thermal resistance by up to 40%. Our previous work has shown that the magnitude of G changes significantly for ultra-small (∼2 nm) interlayer thicknesses and that its thickness dependence saturates at different values according to the EPC strength of the interlayer [21]. It has become clear that key parameters that influence the interfacial heat transport in a well-bonded metal-dielectric system are the EPC of the metallic layers and the phonon spectra of the materials in the system. However, the interplay between various contributions involved in thermal transport to total thermal boundary conductance in the presence of an ultrathin (<10 nm) metallic interlayer is not well understood, since different parallel energy transfer pathways may exist when interlayers are thin. This regime is of technological importance, since the overall performance of devices may depend on a compromise between thermal transport and other metrics, such as electrical or optical performance. As an example, plasmonic devices used in heat-assisted magnetic recording should include a low-loss plasmonic material but also dissipate heat effectively [1]. Ultra-thin interlayers can therefore facilitate heat dissipation at the interface between a plasmonic metal and a dielectric heat sink provided that its thickness is small enough to not introduce additional plasmonic losses. This work focuses on determining whether the Debye temperature is a good metric to predict G at metal-dielectric interfaces with an ultra-thin metal interlayer, and if increasing the EPC of the interlayer always results in better conductance. The rationale underlying these principles is outlined next.

2. Interlayer selection

The thermal transport between a metal and a dielectric is primarily controlled by phonons, as these carry energy in both materials. When the phonon energies in these materials are different, phonon transmission is hindered due to lack of available phonon states, though inelastic phonon scattering can somewhat increase phonon transmission. It has been argued that phonon interaction at a metal-dielectric interface can be enhanced by adding an interlayer with intermediate vibrational properties in order to bridge the vibrational spectra mismatch of metal and dielectric layers [17, 20]. The vibrational overlap can be expressed in terms of phonon density of states overlap, which determines the number of available phonon states in a determined energy interval. Neglecting momentum conservation or inelastic processes, matching the spectral distribution of the phonon density of states yields a high boundary conductance, since phonons states of the same energy coexist in both materials. Alternatively, since the shape of the spectral density of states for acoustic phonons share common features, one can simply consider the overlap between phonon acoustic cut-off frequencies (ν_A)—these are the maximum phonon frequencies near the Brillouin zone edge. Again, neglecting momentum conservation and inelastic processes,

materials with matching acoustic phonon cut-off frequencies would have similar phonon energies and group velocity, yielding a high boundary conductance. Optical phonons are usually neglected, since acoustic phonon modes have larger group velocities and hence carry most of the heat. Furthermore, high-energy optical phonon modes are not populated in large numbers near or below room temperature. However, there has been evidence to show that optical phonons indeed carry a non-negligible amount of heat [22], and there are some cases where low-lying optical phonons should be considered, as we will also see below.

The Debye approximation assumes linear phonon dispersions ($\nu = cq/(2\pi)$), and the phonon density of states is given by:

$$D(\nu) = \frac{6\nu^2}{c^3} \tag{1}$$

where ν is the phonon frequency and c is the speed of sound. This is valid up to ν_D, which is the Debye cut-off frequency [23]. ν_D is directly proportional to the Debye temperature θ_D ($\nu_D = \hbar\theta_D/(2\pi k_B)$), where $\hbar$ is the reduced Planck's constant and k_B is the Boltzmann constant. Thus, under the linear approximation, the Debye temperature is a direct measure of phonon density of states. Jeong *et al* [14] shows that inserting interlayers with intermediate θ_D enhances the overall thermal boundary conductance at a highly mismatched metal-dielectric interface thanks to the presence of phonon states with intermediate energies. The availability of more phonon modes enhances the phonon flux across the system, resulting in an enhancement in the overall boundary conductance. The use of the Debye approximation is debatable, since realistic phonon dispersions are associated with maximum phonon frequencies near the Brillouin zone edge that are lower than ν_D of the Debye model. This lowers the group velocities near the Brillouin zone edge and the phonon flux through an interface for a specific phonon mode, since the flux is directly proportional to the group velocity and the number of available phonons in that mode. A mismatch in phonon cut-off frequency ν_A lowers the phonon transmission across an interface due to the limit in the available high-energy phonons for transmission [17]. This is not easily captured by comparing Debye temperatures, since realistic phonon dispersions are not simple linear extrapolations of the behavior near the Brillouin zone center. The difference can be further highlighted by considering the following examples. Crystalline SiO_2 has values for θ_D and ν_A of 470 K and 2.5 THz, respectively. For Al, θ_D is 428 K (91% the value of quartz), and ν_A is 7 THz (280% the value of quartz). So, the values do not scale linearly as expected in the linear Debye model. Similarly, Al_2O_3 and Cr have similar cut-off frequencies (7.9 THz each), however the Al_2O_3 Debye temperature is 166% that of Cr. Hence, the phonon cut-off frequency should be a better measure of phonon transport across an interface, as it explicitly gives a limit to the phonon energies involved in the transport.

For the case of metal-dielectric interfaces, it is also important to consider the role of electron–phonon energy transfer because electrons are the primary heat carriers in metals. The EPC constant g of a metal determines the rate of energy exchange between electrons and phonons. Upon the establishment of a temperature gradient, the non-equilibrium between electrons and phonons can be long-lived if the metal has a weak g. This increases the resistance to heat transport across a metal-dielectric interface, since energy transfer needs to bridge the electron system (which dominates transport in a metal) and the phonon system (which is the sole energy carrier in a dielectric), yielding an overall reduction of the thermal boundary conductance G. Adding an interlayer with higher g at the metal-dielectric interface can decrease the non-equilibrium by rapidly dragging the electron and phonon systems into equilibrium [15, 18, 19]. It is not clear, however, whether g of the interlayer can be arbitrarily large or whether it plays a role with respect to other thermophysical properties of the system.

In order to understand the role of these parameters and determine the driving mechanisms for the modification of G at a metal-dielectric interface, we analyze a series of interfaces in the presence of various interlayers with a thickness of 5 nm. The thickness was chosen based on our previous work, so that the thickness-dependence of the interlayer would not be a factor even when considering materials with differing g, allowing us to focus on the material properties and decouple any effects of the interlayer thickness [21]. Interlayers were selected based on the assumption that adding an interlayer with intermediate vibrational properties and higher EPC constant should enhance the overall thermal boundary conductance. It should be noted that for the interlayer thickness used in this work (5 nm), the rationale of using an intermediate Debye temperature is less applicable, as we show that at this thickness the interlayer material properties dominate the transport, and the properties of the top metal are less important. However, we will show that material choices based on the Debye picture are still less reliable in determining the thermal boundary conductance. We consider three material parameters in our analysis: Debye temperature (θ_D), acoustic phonon cut-off frequencies (ν_T and ν_L for transverse and longitudinal modes, respectively), and volumetric EPC constant (g). To understand the role of each parameter, we fabricated a matrix of metal-interlayer-dielectric systems as shown in table 1. The first column represents the interlayer parameters whose influence is being tested. The second column represents the corresponding choice of top metal and dielectric substrate considered. The third column represents the choice of interlayer inserted between metal and dielectric. The various thermophysical properties of materials used in this study are given in table 2.

The values for Debye temperature or phonon cut-off frequency may not be readily available for the materials of interest. The Debye temperature can be determined experimentally from the longitudinal & transverse speeds of sound or bulk modulus & Poisson ratio, or theoretically from the phonon dispersion curves. Knowledge of the phonon dispersion curves is required to determine the phonon cut-off frequencies, and this can be obtained experimentally through neutron or x-ray scattering or theoretically through ab-initio methods or lattice dynamics. Generally speaking, the accessibility of lattice dynamics simulations facilitates the determination of phonon dispersions, so that accessing values for phonon cut-off frequencies is relatively straightforward

Table 1. Metal-interlayer-dielectric sample sets analyzed in this work. Samples exploring the tabulated combinations of metal-interlayer-dielectric materials were considered to determine the influence of the parameter of interest indicated. Metals were 50 nm thick and interlayers 5 nm thick.

Parameter of interest	Metal-X-dielectric structure (X is the interlayer)	Metallic interlayer
Debye temperature (θ_D)	Al-X-Al_2O_3 Al-X-SiO_2	Cr Ni
Volumetric electron–phonon coupling constant (g)	Au-X-Al_2O_3 Al-X-Al_2O_3	Al Cr Ni
Acoustic phonon cut-off frequencies (ν_T and ν_L)	Au-X-AlN Au-X-Al_2O_3	Cr Ni

Table 2. Thermophysical properties of different materials of interest in this work. θ_D is the Debye temperature, ν_L, ν_T, ν_A and ν_{optical} are highest phonon frequencies for the longitudinal acoustic modes, two transverse acoustic modes, polarization-averaged acoustic modes and optical modes, respectively. g is the volumetric electron–phonon coupling constant.

Top metal	Interlayer	Substrate
Al $\theta_D = 428$ K [30] $\nu_L = 9.6$ THz [38] $\nu_T = 5.7$ THz [38] $\nu_A = 7$ THz $g = 0.24 \times 10^{18}$ W $(m^3 \cdot K)^{-1}$ [30]	Al $\theta_D = 428$ K [30] $\nu_L = 9.6$ THz [38] $\nu_T = 5.7$ THz [38] $\nu_A = 7$ THz $g = 0.24 \times 10^{18}$ W $(m^3 \cdot K)^{-1}$ [30]	AlN $\theta_D = 1150$ K [37] $\nu_L = 17.6$ THz [39] $\nu_T = 10.3$ THz [39] $\nu_A = 12.7$ THz $\nu_{\text{optical}} = 27$ THz [39]
Au $\theta_D = 165$ K [30] $\nu_L = 4.6$ THz [41] $\nu_T = 2.8$ THz [41] $\nu_A = 3.4$ THz $g = 0.023 \times 10^{18}$ W $(m^3 \cdot K)^{-1}$ [30]	Cr $\theta_D = 630$ K [33] $\nu_L = 10$ THz [42] $\nu_T = 6$ THz, 7.7 THz [42] $\nu_A = 7.9$ THz $g = 0.42 \times 10^{18}$ W $(m^3 \cdot K)^{-1}$ [44]	c-Al_2O_3 $\theta_D = 1047$ K [40] $\nu_L = 10$ THz [43] $\nu_T = 6.9$ THz [43] $\nu_A = 7.9$ THz $\nu_{\text{optical}} = 26$ THz [43]
	Ni $\theta_D = 450$ K [30] $\nu_L = 9.1$ THz [46] $\nu_T = 4.5$ THz [46] $\nu_A = 6$ THz $g = 0.36 \times 10^{18}$ W $(m^3 \cdot K)^{-1}$ [30]	α-SiO_2 $\theta_D = 470$ K [45] $\nu_L = 4$ THz [47] $\nu_T = 1.8$ THz [47] $\nu_A = 2.5$ THz $\nu_{\text{optical}} = 37$ THz [47]
	Ta $\theta_D = 225$ K [48] $\nu_L = 5.5$ THz [42] $\nu_T = 2.6$ THz, 3.7 THz [42] $\nu_A = 3.9$ THz $g = 3.1 \times 10^{18}$ W $(m^3 \cdot K)^{-1}$ [51]	Si $\theta_D = 640$ K [49] $\nu_L = 12$ THz [50] $\nu_T = 4.6$ THz [50] $\nu_A = 7.1$ THz $\nu_{\text{optical}} = 16$ THz [50]

even for materials that are not well characterized in the literature.

3. Experiment

The metal bilayers were deposited on α-SiO_2, c-Al_2O_3 or Si single crystal substrates by dc-magnetron sputtering in an argon atmosphere with a gas pressure of 3 m Torr (base pressure of better than 10^{-8} Torr). The deposition rates for Al, Au, Ni and Cr are 0.6 Å s^{-1}, 1.5 Å s^{-1}, 0.5 Å s^{-1}, 1.7 Å s^{-1}, respectively. For the AlN samples, we used commercial Al_2O_3 substrates with a 1 μm epitaxially grown AlN layer. Top metal layers of Al or Au are ∼50 nm thick, and the interlayers, when present, are ∼5 nm thick unless otherwise noted for the thickness-dependent study. X-ray reflectivity (XRR) was used to measure the actual thickness of the layers and this measurement was used in the thermal model. The resulting metal bilayers exhibit similar degrees of polycrystallinity among the samples, as evidenced by the structures we reported previously that were grown in the same conditions [24, 25]. The crystallinity tends to evolve with the film thickness, so for interlayer metals having the same thickness the crystallinity would be very comparable, and therefore this would not play

an important role in the transport. The interfaces created in this way have been characterized to be sharp with practically no intermixing [25].

We used time-domain thermoreflectance (TDTR) to measure the thermal boundary conductance between metal layers and substrates [5, 26]. TDTR uses an ultrafast optical pump pulse to heat up the surface of the sample and subsequently a time-delayed probe pulse measures the change in temperature as a function of pump-probe delay. The pump and probe beams were generated at 515 nm and 1030 nm from an ultrafast fiber laser and second harmonic generator (Amplitude Laser, Satsuma HP^2) with a pulse width of 350 fs and repetition rate of 40 MHz. The experiments were performed at 1–3 MHz modulation frequency using pump and probe $1/e^2$ radii of 7.7 μm and 4.8 μm respectively. To obtain quantitative results for interface thermal conductance and substrate thermal conductivity, we fit the experimental results with a thermal transport model based on the solution of the heat diffusion equation in cylindrical symmetry on layered media [27]. For fitting purposes, the metallic bilayer is considered as a single layer having a thickness equal to the total bilayer thickness and volumetric heat capacity equal to the thickness-weighted value [14]. This does not introduce significant error as the sensitivity to the thermal resistance of these metallic layers is far smaller than the sensitivity to boundary conductance. The model assumes that all the heat is deposited on the surface of the top metal layer, which is not strictly accurate. However, for the top metals used in this work, the optical penetration depths at the optical wavelengths used are below 20 nm, well below the thickness of the top metal. Furthermore, when accounting for the finite optical absorption of the light, the fitted values reported do not change significantly [27]. The thermal conductivity of the bilayer was obtained through the Wiedemann–Franz Law and four-point-probe measurements of the electrical conductivity of the metallic films. All volumetric heat capacity values were obtained from the literature. The thermal conductivity of the substrates were left as free fitting parameters for the samples without interlayers and the obtained values did not deviate from accepted literature values for the bulk crystals within the experimental error. A Monte Carlo approach was used to estimate the error propagation associated with the thermophysical properties that were assumed constant and the experimental noise [28]. The parameters and 1 σ uncertainties varied in the Monte Carlo simulation were: the thickness of the metal layer (based on the uncertainty of the XRR measurements), the thermal conductivity of the metal layer (10%), the optical spot size (2%), the thermal conductivity of the substrates (8% for Al_2O_3 and 11% for silicon) and the phase noise of the TDTR measurement (0.1–0.5 degrees, estimated from the phase noise in each measurement).

4. Results and discussion

4.1. Thickness dependence of the interlayer

Before discussing the main results of this work, we discuss an interlayer thickness-dependence study for the Au/Ni/Al_2O_3 system to verify that the thermal boundary conductance saturates for a thickness of 5 nm as expected, in order to justify the use of a constant 5 nm interlayer thickness for the following samples in this work. The study was done by inserting ultrathin layers (0.5 nm–5 nm) of Ni at the interface of Au/Al_2O_3 and measuring the thermal boundary conductance. Our previous study [21] showed that the thickness dependent thermal boundary conductance at a metal-dielectric interface reaches a saturation before ∼5 nm if the interlayers have a sufficiently strong EPC constant. This thickness-dependent study also demonstrates the use of our theoretical model to predict the saturation thickness for the interlayers used in this study.

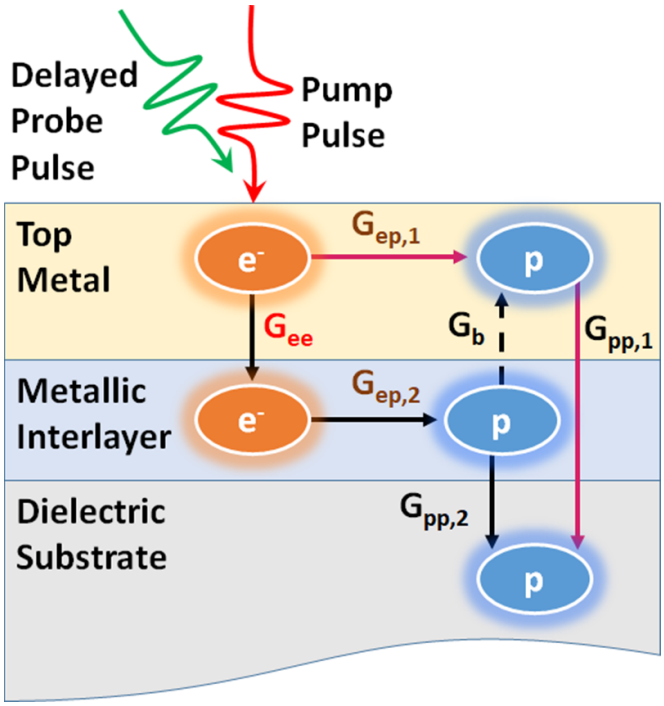

Figure 1. Thermal transport mechanisms at a metal-dielectric interface in the presence of an interlayer. Red and black solid arrows represent heat transport *pathway 1* and *pathway 2*, respectively. The black dashed arrow represents heat backflow from the interlayer to the top metal. In this work, *pathway 2* dominates transport, since the interlayers studied are 5 nm thick.

In order to model the overall thickness dependence of G in a metal-interlayer-dielectric system, we previously developed a thermal model of interface transport based on the main transport pathways shown in figure 1 [21]. The total interfacial conductance involves two parallel heat transfer pathways. *Pathway 1* accounts for the thermal conductance due to initial electron–phonon energy exchange ($G_{ep,1}$) in the top metal layer and subsequent phonon–phonon energy transfer between phonons in the top metal layer with phonons in the substrate ($G_{pp,1}$). This process bypasses transport in the interlayer by assuming that phonons having a longer wavelength than the interlayer thickness can directly tunnel to the dielectric, and as the thickness of the interlayer increases, the contribution of long wavelength phonons from the top metal layer decreases, reducing the phonon flux for this pathway. The total interfacial conductance G_1 in *pathway 1* due to the two energy transfer

processes can be expressed assuming the conductance due to both mechanisms is in series:

$$\frac{1}{G_1} = \frac{1}{G_{\mathrm{ep},1}} + \frac{1}{G_{\mathrm{pp},1}}. \tag{2}$$

For the top metal layer, the conductance $G_{\mathrm{ep},1} = \sqrt{k_p g}$, where k_p is the phonon contribution to the thermal conductivity in the metal.

In *pathway 2*, electrons in the top metal layer interact with the electrons in the metallic interlayer (G_{ee}) [29], and subsequently, these electrons transfer their energy to the lattice. The thickness-dependent volumetric energy exchange between electrons and phonons in the thin interlayer can be expressed as $G_{\mathrm{ep},2} = hg$ where, h is the interlayer thickness. Heat from the interlayer can then transfer to the dielectric ($G_{\mathrm{pp},2}$) or can propagate back to the top metal (G_b) depending on the electron–phonon coupling constant of the interlayer and the time-dependent temperature dynamics of the system. Back-propagation through G_b can be neglected as this transfer mechanism is only relevant for time scales shorter than the ones we analyze in the TDTR response (less than 10 ps). The total interface conductance G_2 due to pathway 2 can be expressed as:

$$\frac{1}{G_2} = \frac{1}{G_{\mathrm{ee}}} + \frac{1}{G_{\mathrm{ep},2}} + \frac{1}{G_{\mathrm{pp},2}} \tag{3}$$

Similarly to *pathway 1*, contributions to $G_{\mathrm{pp},2}$ in the interlayer are only considered for phonons having shorter wavelength than the physical interlayer thickness.

To model the phonon–phonon conductances $G_{\mathrm{pp},1}$ and $G_{\mathrm{pp},2}$ in the system, we used a modified version of the diffuse mismatch model (DMM) described in detail in [21]. Briefly, we used realistic phonon dispersions for the materials considered and limit the integration according to phonon wavelength λ and layer thickness as needed:

$$G(\lambda)_{\mathrm{pp}} = -\frac{1}{8\pi^2}\sum_{j,A}\int_{\lambda_{\min}}^{\lambda_{\max}} h\nu_{j,A}q_{j,A}^2\,|\upsilon_{j,A}|\,\alpha_{A\to B}\frac{\mathrm{d}f_{\mathrm{BE}}}{\mathrm{d}T}\frac{2\pi}{\lambda^2}\mathrm{d}\lambda_{j,A} \tag{4}$$

where h is Planck's constant, $\nu_{j,A}$ are the phonon frequencies for branch j in material A, υ is the group velocity, $f_{\mathrm{BE}} = 1/\left[\exp\left(h\nu_{j,A}/k_BT\right) - 1\right]$ is the Bose–Einstein distribution and the integration is limited between the shortest phonon wavelength at the Brillouin zone edge $\lambda_{\min}$ and $\lambda_{\max}$ is limited to the interlayer thickness. We refer the reader to the supplementary information for the phonon dispersion curves for the materials used in this study. Given that the inelastic contribution to phonon transmission is only likely to take place for low-n phonon processes [23], during the calculations of the transmission coefficients we employ a hybrid approach where we consider elastic processes for the energetically mismatched Au/Al_2O_3 interface (where high-n phonon processes are unlikely) and inelastic processes for the better matched Ni/Al_2O_3 interface (where low-n phonon processes are likely). Here we refer to low-n phonon processes as inelastic scattering processes involving few (3–4) phonons. In practice, we distinguish our hybrid DMM model in three cases: (a) when acoustic modes of materials across the interface have energies within a factor of 2, as in the Al/Si system, we consider inelastic scattering, since these would involve few-phonon processes and are more likely; (b) when acoustic modes differ by more than a factor of 2 as in Ta/Si (the cut-off frequency of the LA mode of Si is more than 2× that of the LA mode of Ta), we consider elastic scattering, since it is not as likely to have many inelastic processes involving phonons that could span large energy differences; (c) when the acoustic modes of the metal are comparable to those of the dielectric, but there are low-lying optical modes of comparable energies, as in the Al/Al_2O_3 system, we consider inelastic scattering as in case (a) but also include low-lying optical modes of the dielectric that have comparable frequencies to those of the metal. Elastic versus inelastic scattering is considered as previously described [21], and take the form

$$\alpha_{A\to B,\mathrm{elastic}} = \frac{\sum_{j,B} h\nu_{j,B}q_{j,B}^2\upsilon_{j,B}f_{\mathrm{BE}}}{\sum_{j,B} h\nu_{j,B}q_{j,B}^2\upsilon_{j,B}f_{\mathrm{BE}} + \sum_{j,A} h\nu_{j,A}q_{j,A}^2\upsilon_{j,A}f_{\mathrm{BE}}} \tag{5}$$

$$\alpha_{A\to B,\mathrm{inelastic}} = \frac{\sum_{j,B}\int h\nu_{j,B}q_{j,B}^2\upsilon_{j,B}f_{\mathrm{BE}}\mathrm{d}q_{j,B}}{\sum_{j,B} h\nu_{j,B}q_{j,B}^2\upsilon_{j,B}f_{\mathrm{BE}}dq_{j,B} + \sum_{j,A} h\nu_{j,A}q_{j,A}^2\upsilon_{j,A}f_{\mathrm{BE}}\mathrm{d}q_{j,A}} \tag{6}$$

Briefly, the transmission probability in the elastic case is calculated as the fraction of heat flux across the interface as function of the wave-vector, thereby forcing the correspondence of phonon energies on either side of the interface at each wave-vector for transmission to occur. In the inelastic case the fraction of heat flux across the interface is calculated by integrating over all the heat flux contributions, thereby considering all possible carrier scattering initial and final states.

The total thermal boundary conductance in the material due to the two pathways can be calculated assuming that they are in parallel:

$$G_{\mathrm{model}} = G_1 + G_2 \tag{7}$$

Figure 2 shows the thermal boundary conductance for the Au/Ni/Al_2O_3 system as a function of interlayer thickness. The symbols represent the measured G, and the black and red curves show the G calculated from the model above, with and without the contribution of the low-frequency quasi-optical phonons in Al_2O_3, respectively. We plot two sets of curves: the solid lines use the EPC of Ni of 0.36×10^{18} W $(\mathrm{m}^3\cdot\mathrm{K})^{-1}$, but for reference we include in the dashed lines the EPC value of 1.03×10^{18} W $(\mathrm{m}^3\cdot\mathrm{K})^{-1}$. This is because previous studies have reported multiple values for g of Ni in the above range [30]. From the figure, we can conclude that only low-frequency quasi-optical phonons in Al_2O_3 contribute to the thermal boundary conductance, as it is unlikely that high n-phonon processes would be involved or that high-energy optical phonon modes would be occupied near room temperature. The experimental G evolution trend saturates at

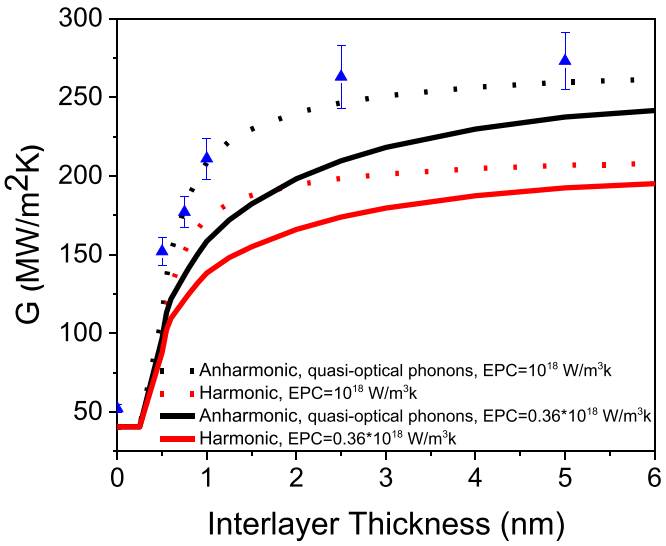

Figure 2. Comparison of experimental G with the model as function of interlayer thickness for the Au/Ni/Al_2O_3 system. Experimental results are represented as filled symbols. The red solid curve represents the total G evolution based on the hybrid model including only acoustic phonons in Al_2O_3 with Ni EPC $= 0.36 \times 10^{18}$ W $(m^3 \cdot K)^{-1}$. The black solid line denotes the hybrid model considering low-frequency quasi-optical phonon modes in Al_2O_3 with Ni EPC $= 0.36 \times 10^{18}$ W $(m^3 \cdot K)^{-1}$. The dotted lines represent the G evolution with Ni EPC value of 10^{18} W $(m^3 \cdot K)^{-1}$.

5 nm as expected. Other interlayers used later in this study are Al, Cr and Ta, the first two having a similar EPC value to Ni, and Ta having a much higher value. Cr and Ta interlayers are expected to have a thickness dependence that saturates similarly to or even more quickly than Ni, but for Al, having a smaller EPC, more attention is needed. This case will be discussed in more detail in the section on the role of the electron–phonon coupling. The results so far tell us that for most materials studied here a 5 nm interlayer thickness is sufficient to saturate the value for G due to the sufficiently high electron–phonon coupling values of the interlayers. The overall predicting ability of our hybrid DMM model for the samples studied in this work is provided in the supplementary information, where we show that the modeled value for G is typically within 30%, save a few outliers.

4.2. Role of vibrational properties

We now proceed to compare G across several metal/interlayer/dielectric interfaces to determine whether the Debye temperature or phonon cut-off frequency is a better predictor. We analyzed three different substrates with different phonon cut-off frequencies providing different phonon flux at the interface with the metals. The substrates used are AlN ($\theta_D = 1150$ K) and Al_2O_3 ($\theta_D = 1047$ K) with similar Debye temperatures, as well as SiO_2 ($\theta_D = 470$ K), with a much lower Debye temperature. Note that the longitudinal acoustic phonon modes of these substrates reach 17.6, 10 and 4 THz, respectively, at the Brillouin zone edge, and therefore AlN and Al_2O_3 are vibrationally more dissimilar than a comparison of Debye temperature would at first suggest. This comparison is done in figure 3.

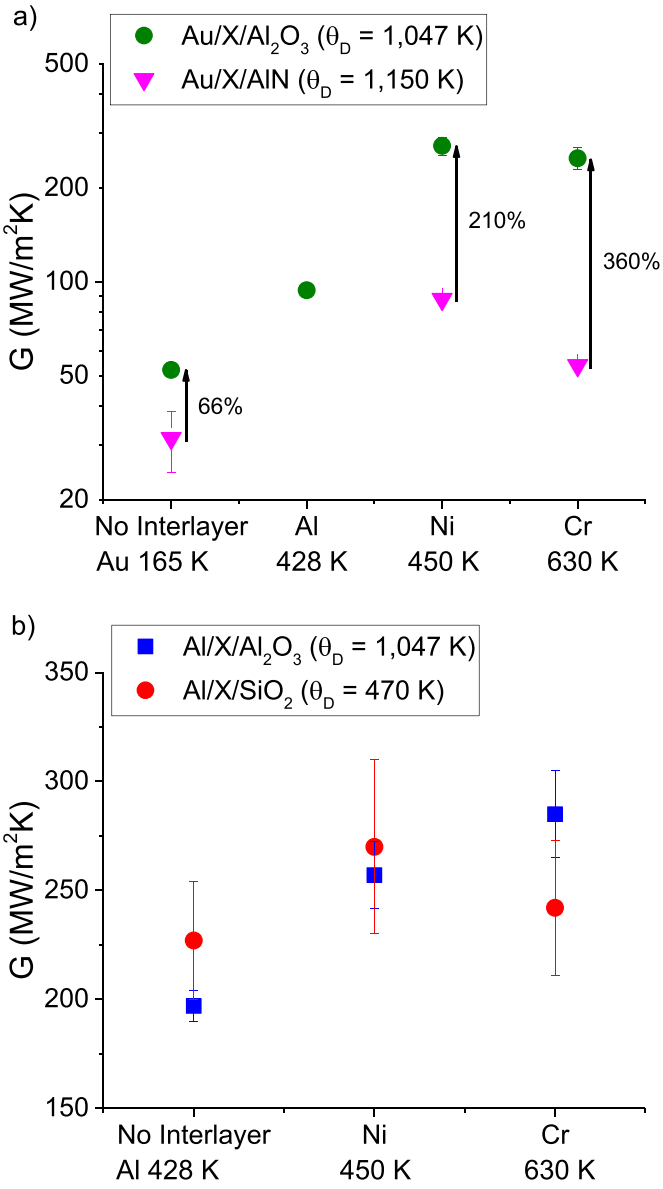

Figure 3. (a) Experimentally measured thermal boundary conductance for Au on various interlayers on Al_2O_3 or AlN substrate (log scale). There is a large dependence on substrate material, even though their θ_D values are similar. (b) Similar comparison for Al on Al_2O_3 and SiO_2 (linear scale). There is no large dependence on substrate material, even though their θ_D values are very different.

The measured thermal boundary conductance for the Au/Al_2O_3 system was 52 MW m^{-2} K^{-1} and in the presence of 5 nm Al, Ni or Cr interlayers, the measured thermal boundary conductance increased to 94, 273 and 249 MW m^{-2} K^{-1}. For the Au/Al_2O_3 system, the presence of interlayers enhanced the thermal boundary conductance significantly with the highest change being observed for Ni (425%). Inserting Ni and Cr with intermediate Debye temperature at Au/AlN changed the measured thermal boundary conductance value from 32 MW m^{-2} K^{-1} to 88 and 54 MW m^{-2} K^{-1}, respectively. Similarly to the Au/interlayer/Al_2O_3 sample set, the

enhancement is highest for the Ni interlayer (175%). As shown in figure 3(a), comparing the magnitude of thermal boundary conductance between Au/AlN and Au/Al_2O_3 clearly shows that despite the similar Debye temperature between Al_2O_3 and AlN, the magnitude of G is higher for Au/Al_2O_3 set (up to a factor of almost 4×). This observation shows that a similarity in Debye temperatures is not a good predictor of thermal boundary conductance. However, we will show that the higher magnitude of G for Au/interlayer/Al_2O_3 system can be better predicted based on the improved overlap of acoustic phonons in Al_2O_3 with respect to the top metal phonons, as opposed to the case for metal/AlN interfaces.

As a further example, we compare the performance on Al_2O_3 and SiO_2 substrates in figure 3(b). We inserted a 5 nm Ni or Cr interlayers at the Al/Al_2O_3 interface, yielding an overall measured thermal boundary conductance of 197 MW $m^{-2} K^{-1}$ for the bare Al/Al_2O_3 interface, and 257 and 285 MW $m^{-2} K^{-1}$, for the Ni and Cr interlayers, respectively. The measured thermal boundary conductance for Al/Al_2O_3 is ∼200 MW $m^{-2} K^{-1}$, in good agreement with previously reported values [17, 31–33]. The slight variations can be due to the presence of residual impurities on the surface of the substrate. For the SiO_2 substrate having an Al/SiO_2 thermal boundary conductance of 227 MW $m^{-2} K^{-1}$, the addition of Ni and Cr interlayers altered the thermal boundary conductance to 270 and 242 MW $m^{-2} K^{-1}$, respectively. Despite the highly dissimilar Debye temperature of Al_2O_3 and SiO_2 (1047 K and 470 K, respectively), the measured thermal boundary conductance values of various metal/SiO_2 interfaces are similar to the metal/Al_2O_3 ones. This trend shows that the magnitude of the thermal boundary conductance for the metal-dielectric system cannot be predicted based on the mismatch between the Debye temperatures of the materials involved.

The lower thermal boundary conductance value in the metal/AlN system can be attributed to low phonon flux and transmission due to the weak spectral overlap between metal phonon modes and those in AlN. This poor phonon match can be deduced from the differences in acoustic phonon cut-off frequencies in table 2. Generally, the metal/Al_2O_3 and metal/SiO_2 systems offer better conductance, as most metals have similar phonon frequencies. Since acoustic phonon modes have three polarizations, for simplicity we compare the polarization-averaged phonon cut-off frequencies, by averaging the values for the two transverse and one longitudinal polarizations, $\nu_A = (\nu_{T1} + \nu_{T2} + \nu_L)/3$. The relatively higher difference in cut-off frequency between AlN ($\nu_A = 12.7$ THz) and metals (e.g. Ni:$\nu_A = 6$ THz) decreases the phonon flux at the interface. The probability of higher-order inelastic processes contributing to thermal transport decreases with the number of participating phonons, so we would not expect a significant contribution from optical phonons unless they have similar energies to the acoustic modes. For Al_2O_3 ($\nu_A = 7.9$ THz) the acoustic phonon cut-off frequencies are closer to Cr ($\nu_A = 7.9$ THz) followed by Al ($\nu_A = 7$ THz) and Ni ($\nu_A = 6$ THz). The measured thermal boundary conductance in the Al/Al_2O_3 set showed higher thermal boundary conductance for Al/Cr/Al_2O_3 followed by Al/Ni/Al_2O_3 and Al/Al_2O_3. For SiO_2 ($\nu_A = 2.5$ THz), one might at first expect

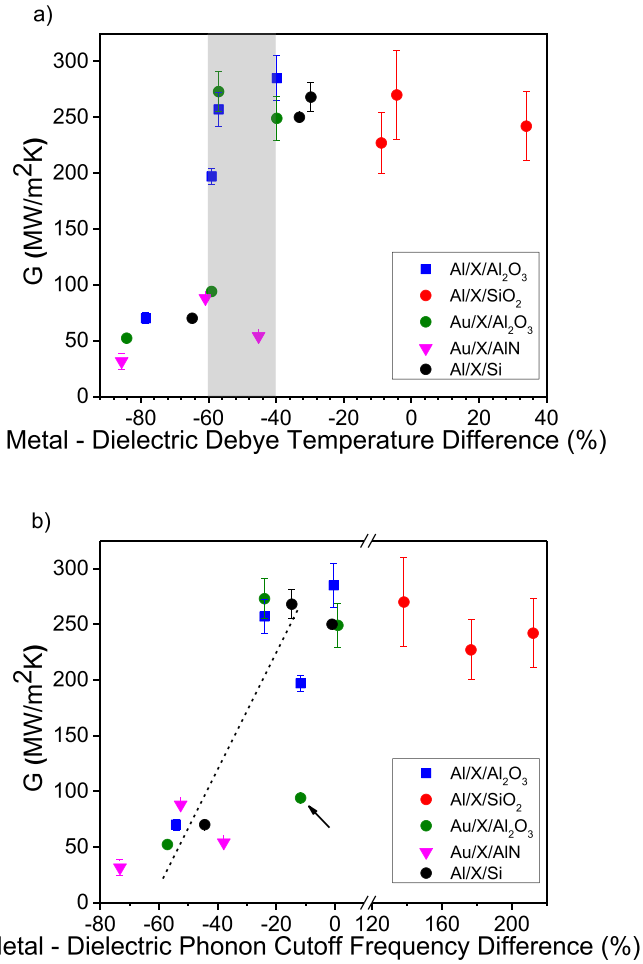

Figure 4. (a) Experimentally measured thermal boundary conductance data as function of percent difference in θ_D between contacting metal layer and substrate. The difference in θ_D is not very predictive of G, since the shaded area with a mismatch of 40%–60% yields values for G spanning a large range. (b) Same data plotted as function of percent difference in average acoustic phonon cut-off values ν_A between contacting metal layer and substrate. The dotted line is a guide to the eye. The trend supports the idea that similar acoustic phonon cut-off values lead to higher values for G. The most significant outlier indicated by the arrow is for the Au/Al/Al_2O_3 sample, which is discussed in the text. The data in panels (a) and (b) are tabulated in table 3.

a lower G, because the phonon cut-off frequencies are lower than those of most metals. However, SiO_2 has several low-lying optical phonon branches below 10 THz, and these may match well the phonon modes of the metals through elastic or low-order inelastic scattering. AlN and Al_2O_3, on the other hand, do not have such low-lying optical phonon branches. These observations indicate that phonon cut-off frequency may be a better quantity to explain the trend and magnitude of thermal boundary conductance at a metal/dielectric interface in the presence of an interlayer.

To further reinforce this argument, figure 4 compares our data within the Debye temperature or phonon cut-off frequency models. Here we test whether a better match in Debye temperatures or phonon cut-off frequencies can explain our data. To illustrate this, we define the relative

Table 3. Measured G for metal-interlayer-dielectric samples analyzed in this work, together with percent difference in θ_D or ν_A between contacting metal and substrate.

Metal-X-dielectric structure (X is the interlayer)	Metallic interlayer	Metal-dielectric θ_D difference (%)	Metal-dielectric ν_A difference (%)	G (MW m^{-2} K^{-1})
Al-X-Al_2O_3	—	−59.1	−11.7	197 ± 7
	Ta	−78.5	−54.2	70 ± 5
	Cr	−39.8	0	285 ± 20
	Ni	−57.0	−24.0	257 ± 15
Al-X-SiO_2	—	−8.9	+176.7	227 ± 27
	Cr	+34.0	+212.3	242 ± 31
	Ni	−4.3	+138.3	270 ± 40
Au-X-Al_2O_3	—	−84.2	−57.1	52 ± 2
	Al	−59.1	−11.7	94 ± 1
	Cr	−39.8	0	249 ± 20
	Ni	−57.0	−24.0	273 ± 18
Au-X-AlN	—	−85.7	−73.3	32 ± 7
	Cr	−45.2	−37.9	54 ± 1
	Ni	−60.9	−52.6	88 ± 2
Al-X-Si	—	−33.1	−1.4	250 ± 2
	Ta	−64.8	−44.4	70 ± 2
	Ni	−29.7	−14.7	268 ± 13

difference in metal—dielectric properties as follows: for the Debye temperature the relative difference can be expressed as $(\theta_{DM} - \theta_{DS})/\theta_{DS}$, where θ_{DM} and θ_{DS} are the Debye temperatures of the contacting metal and substrate, respectively. For the cut-off frequency the relative difference is expressed similarly, as $(\nu_{AC} - \nu_{AS})/\nu_{AS}$, where ν_{AC} and ν_{AS} are the values of ν_A for the contacting metal and substrate. Figure 4(a) shows that G does not universally increase when the Debye temperatures become similar as one might expect, with samples having a 45%–60% difference in θ_D showing values for G ranging from below 100 to above 250 MW m^{-2} K^{-1}. Figure 4(b), however, shows a more consistent trend in the data, where the values for G increase as the relative difference in ν_A decreases. The most significant outlier in figure 4(b) indicated by the arrow for the Au/Al/Al_2O_3 sample deviates from the general trend due to insufficiently strong EPC in Al, discussed in more detail in the next section. Referring to the Al/Al_2O_3 sample, which does not include EPC effects the value for G is near 200 MW m^{-2} K^{-1}, in line with the trend. We note again that the mismatch one might expect being associated with lower G for the metal/SiO_2 samples is not present due to low-lying optical modes that significantly contribute to heat transport. We conclude that ν_A is a better parameter to select a metal layer with desired thermal boundary conductance than θ_D, noting that low-lying optical modes must be considered where present, and that for most cases involving interlayers thicker than ∼5 nm, one may simply disregard the influence of a top metal layer.

4.3. Role of electron–phonon coupling constant

We will now turn to the effect the EPC has on G for the samples in this study. Figure 5 plots G for the Au/interlayer/Al_2O_3 and Al/interlayer/Al_2O_3 sample sets as function of the EPC of the contacting metal. The data indicated by arrows represent samples without interlayer, i.e. bare Au/Al_2O_3 and Al/Al_2O_3 interfaces. It is instructive to focus our attention on two comparisons. First, we compare the samples with Al in contact with Al_2O_3:Al/Al_2O_3 with G of 197 MW m^{-2} K^{-1}, and Au/Al/Al_2O_3 with G of 94 MW m^{-2} K^{-1}. One might expect identical results, because the metal-dielectric interface is the same. However, Au possesses a very low EPC, with g of 2.3 × 10^{16} Wm^{-3} K^{-1}, and Al is only 10× larger, causing the electron and phonon thermal baths to

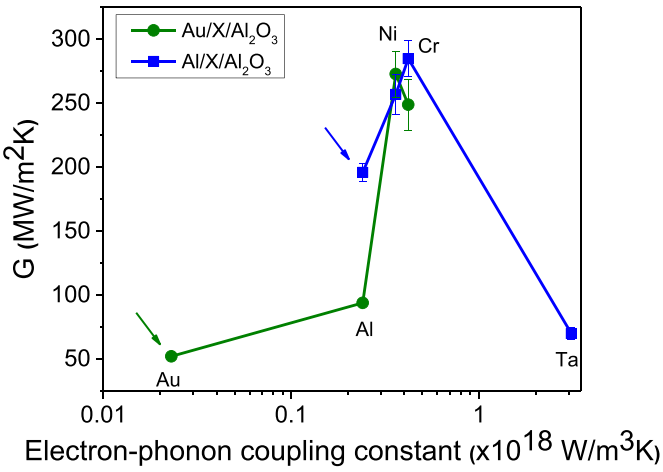

Figure 5. Experimentally measured thermal boundary conductance as a function of electron–phonon coupling constant of the metal in contact with the Al_2O_3 substrate. The arrows indicate data points for simple metal/dielectric samples without interlayer (Au/Al_2O_3 and Al/Al_2O_3).

remain out of equilibrium over a long distance, decreasing the conductance. This can be illustrated through a simple numerical example. Let us first consider the Al/Al_2O_3 interface. Modeling the transport as a series of two resistors modeling the electron to phonon transfer in the Al layer, followed by the phonon–phonon interface, with conductances of $G_{ep,Al} = \sqrt{k_p g} \cong 1.5$ GW m^{-2} K^{-1} and $G_{pp,Al-Sub} = 235$ MW m^{-2} K^{-1} [21], we would predict $G_{Al-Al_2O_3} = 203$ MW m^{-2} K^{-1}, very close to our measured value. The $Au/Al/Al_2O_3$ interfaces can similarly be modeled by a series of resistors modeling the electron to phonon transfer followed by the phonon transport. The length scale for electron–phonon equilibration in the Al layer is $\sqrt{k/g}$ ~30 nm [34], and since this is greater than the Al layer thickness, we can assume that not all electrons would be thermalized. Therefore, one must consider electron–phonon coupling in the Au layer. This leads to considering the following conductances, from top to bottom [35]: $G_{ep,Au} = \sqrt{k_p g} \cong 245$ MW m^{-2} K^{-1}, $G_{pp,Au-Al} = 266$ MW m^{-2} K^{-1} (evaluated by the DMM), $G_{p,Al} = k_p/h \cong 2$ GW m^{-2} K^{-1} and $G_{pp,Al-Sub} = 300$ MW m^{-2} K^{-1}, yielding a predicted $G_{Au-Al-Al_2O_3} = 86$ MW m^{-2} K^{-1}, again close to our measurement. Thus, it is clear that the low EPC in Au and Al causes significant resistance. This is compatible with our model presented in figure 2(b), where the saturation of G occurs at higher interlayer thickness due to the relative weakness of the EPC in Al. For comparison, the $Au/Cr/Al_2O_3$ has an interlayer with an EPC almost 2× that of Al. Assuming that this is sufficient to equilibrate the electron and phonon temperatures in the Cr layer, the conductance predicted for the $Al/Cr/Al_2O_3$ interfaces would be given by $G_{e,Au} = k_e/h \cong 6$ GW m^{-2} K^{-1}, $G_{ee,Au-Cr} \cong 4$ GW m^{-2} K^{-1}, $G_{ep,Cr} = hg = 2$ GW m^{-2} K^{-1} and $G_{pp,Cr-Sub} = 344$ MW m^{-2} K^{-1}, yielding $G_{Au-Cr-Al_2O_3} = 263$ MW m^{-2}K^{-1}, which matches well our experiment. These considerations, while employing approximations in modeling the overall transport, show a good degree of agreement with our experimental data, and can explain why the $Au/Al/Al_2O_3$ sample has a lower conductance then the Al/Al_2O_3 interface, and why the Au/Al bilayer is the interface that is more importantly affected by the value of the EPC.

A second comparison of note in figure 5 is between the Au/Al_2O_3 and $Al/Ta/Al_2O_3$. The G at Au/Al_2O_3 interface measured experimentally was 52 MW m^{-2}K^{-1}. This is in agreement with previously reported Au/Al_2O_3 G values ranging between 50 MW m^{-2}K^{-1}–70 MW m^{-2}K^{-1} [14, 16, 35]. The Au/Al_2O_3 interface is highly resistive due to both large phonon mismatch but also due to the resistance incurred by the high EPC of Au. The $Al/Ta/Al_2O_3$ interface shows a comparable value for G. Although Ta has a very high EPC, and electron–phonon non-equilibrium is not an important factor in the overall interface conductance. Rather, the very large mismatch in phonon frequencies between Ta and Al_2O_3 is responsible for the similar value for G to the Au/Al_2O_3 interface. This highlights that a high EPC will not by itself lower the boundary conductance.

Based on these observations, we suggest that when the electron–phonon non-equilibrium in the top layer is strong for its thickness (such as 50 nm of Al), the overall thermal boundary conductance is primarily governed by phonon frequency overlap between interlayer and substrate. However, when the top metal layer has a weak electron–phonon coupling constant (such as 50 nm of Au), the modification of thermal boundary conductance involves an interplay between phonon spectra overlap and coupling strength of interlayer.

Models based on the DMM typically can estimate the order of magnitude of G [22], but as the complexity of the models have grown, so did their prediction ability. Generally speaking, however, prediction models based on the DMM have their limitations, as they include simplifying assumptions such as the way scattering is modeled at the interface and phonon dispersion. More sophisticated theories such as those based on the Landauer formalism or atomistic Green's function with input from density functional theory can be more accurate if the interfaces are well-controlled [36], but require much more computational investment and are therefore still seldomly used. Despite its limitations, the hybrid DMM model used in our prior work is able to capture the most dominant aspects affecting the value of G (see [21] and supplementary information), and therefore can provide reasonable predictability. As we have shown here, even a relatively simple comparison of acoustic cut-off frequencies can provide a first indication of what interlayers should produce the desired change in G in metal-dielectric systems.

5. Conclusion

We studied the interfacial mechanisms that affect the thermal boundary conductance in metal-dielectric systems in the presence of an interlayer. The two important interlayer properties that determine the modification of G at metal-dielectric interfaces are phonon spectra and electron–phonon coupling strength. Better overlap between phonon spectra of the interlayer and substrate enhances the overall G due to the increase in phonon flux at the interface. The enhancements can be very sizeable, above 3× in the materials studied in this work. Comparing acoustic phonon cut-off frequency is found to be a better metric than Debye temperature in predicting phonon matching at interfaces. The influence of the top metal is not important in most cases (where the top metal EPC is at least as strong as Al) for interlayer thickness of only 5 nm. However, for top metals with very weak EPC such as Au, the overall value for G involves an interplay between phonon spectra overlap and coupling strength of interlayer. The EPC strength of the interlayer determines the thermal boundary conductance saturation thickness in the presence of an interlayer in all metal/dielectric systems. However, the EPC alone cannot be used as a quantity to predict the modification of thermal boundary conductance in the presence of an interlayer.

Data availability statement

The data that support the findings of this study are available upon reasonable request from the authors.

Acknowledgments

S M O and S P acknowledge support by the Natural Sciences and Engineering Research Council of Canada, the Canada Foundation for Innovatio and CMC Microsystems.

ORCID iD

Simone Pisana https://orcid.org/0000-0002-9291-6061

References

[1] Bain J A, Malen J A, Jeong M and Ganapathy T 2018 Nanoscale thermal transport aspects of heat-assisted magnetic recording devices and materials *MRS Bull.* **43** 112
[2] Chen G 2000 Phonon heat conduction in nanostructures *Int. J. Therm. Sci.* **39** 471
[3] Yang R 2006 Nanoscale heat conduction with applications in nanoelectronics and thermoelectrics *PhD Dissertation* Massachusetts Institute of Technology
[4] Goodson K E and Ju Y S 1999 Heat conduction in novel electronic films *Annu. Rev. Mater. Sci.* **29** 261
[5] Hopkins P E 2013 Thermal transport across solid interfaces with nanoscale imperfections: effects of roughness, disorder, dislocations, and bonding on thermal boundary conductance *ISRN Mech. Eng.* **2013** 682586
[6] Majumdar A and Reddy P 2004 Role of electron–phonon coupling in thermal conductance of metal–nonmetal interfaces *Appl. Phys. Lett.* **84** 4768
[7] Hopkins P E and Norris P M 2007 Substrate influence in electron–phonon coupling measurements in thin Au films *Appl. Surf. Sci.* **253** 6289
[8] Lombard J, Detcheverry F and Merabia S 2015 Influence of the electron–phonon interfacial conductance on the thermal transport at metal/dielectric interfaces *J. Phys.: Condens. Matter* **27** 015007
[9] Swartz E T and Pohl R O 1989 Thermal boundary resistance *Rev. Mod. Phys.* **61** 605
[10] Wang Y and Ruan X An evaluation of energy transfer pathways in thermal transport across solid/solid interfaces *ASME 2013 Heat Transfer Summer Conf. Collocated with ASME 2013 7th Int. Conf. Energy Sustainability ASME 2013 11th Int. Conf. Fuel Cell Science Engineering Technology Volume 1: Heat Transfer in Energy Systems; Thermophysical Properties; Theory and Fundamental Research in Heat Transfer* (*Minneapolis, MN, 14–19 July 2013*) p V001T03A041
[11] Duda J C and Hopkins P E 2012 Systematically controlling Kapitza conductance via chemical etching *Appl. Phys. Lett.* **100** 111602
[12] Hopkins P E, Baraket M, Barnat E V, Beechem T E, Kearney S P, Duda J C, Robinson J T and Walton S G 2012 Manipulating thermal conductance at metal-graphene contacts via chemical functionalization *Nano Lett.* **12** 590
[13] Shen M, Evans W J, Cahill D and Keblinski P 2011 Bonding and pressure-tunable interfacial thermal conductance *Phys. Rev.* B **84** 195432
[14] Jeong M, Freedman J P, Liang H J, Chow C M, Sokalski V M, Bain J A and Malen J A 2016 Enhancement of thermal conductance at metal-dielectric interfaces using subnanometer metal adhesion layers *Phys. Rev. Appl.* **5** 014009
[15] Giri A, Gaskins J T, Donovan B F, Szwejkowski C, Warzoha R J, Rodriguez M A, Ihlefeld J and Hopkins P E 2015 Mechanisms of nonequilibrium electron–phonon coupling and thermal conductance at interfaces *J. Appl. Phys.* **117** 105105
[16] Blank M and Weber L 2018 Influence of the thickness of a nanometric copper interlayer on Au/dielectric thermal boundary conductance *J. Appl. Phys.* **124** 105304
[17] Cheaito R *et al* 2015 Thermal boundary conductance accumulation and interfacial phonon transmission: measurements and theory *Phys. Rev.* B **91** 035432
[18] Chen Y P, Wang Y, Li X, Ruan X and Park W 2019 Reducing interfacial thermal resistance between metal and dielectric materials by a metal interlayer *J. Appl. Phys.* **125** 045302
[19] Wang Y, Lu Z, Roy A K and Ruan X 2016 Effect of interlayer on interfacial thermal transport and hot electron cooling in metal-dielectric systems: an electron–phonon coupling perspective *J. Appl. Phys.* **119** 065103
[20] English T S, Duda J C, Smoyer J L, Jordan D A, Norris P M and Zhigilei L V 2012 Enhancing and tuning phonon transport at vibrationally mismatched solid–solid interfaces *Phys. Rev.* B **85** 035438
[21] Oommen S M and Pisana S 2020 Role of the electron–phonon coupling in tuning the thermal boundary conductance at metal-dielectric interfaces by inserting ultrathin metal interlayers *J. Phys.: Condens. Matter* **33** 085702
[22] Duda J C, Beechem T E, Smoyer J L, Norris P M and Hopkins P E 2010 Role of dispersion on phononic thermal boundary conductance *J. Appl. Phys.* **108** 073515
[23] Hopkins P E and Norris P M 2009 Relative contributions of inelastic and elastic diffuse phonon scattering to thermal boundary conductance across solid interfaces *J. Heat Transfer* **131** 022402
[24] Fallarino L, Oelschlägel A, Arregi J A, Bashkatov A, Samad F, Böhm B, Chesnel K and Hellwig O 2019 Control of domain structure and magnetization reversal in thick Co/Pt multilayers *Phys. Rev.* B **99** 024431
[25] Fallarino L, Stienen S, Gallardo R A, Arregi J A, Uhlíř V, Lenz K, Hübner R, Oelschlägel A, Hellwig O and Lindner J 2020 Higher-order ferromagnetic resonances in out-of-plane saturated Co/Au magnetic multilayers *Phys. Rev.* B **102** 094434
[26] Schmidt A J 2008 Optical characterization of thermal transport from the nanoscale to the macroscale *PhD Dissertation* Massachusetts Institute of Technology
[27] Cahill D G 2004 Analysis of heat flow in layered structures for time-domain thermoreflectance *Rev. Sci. Instrum.* **75** 5119
[28] Rahman M, Shahzadeh M and Pisana S 2019 Simultaneous measurement of anisotropic thermal conductivity and thermal boundary conductance of 2-dimensional materials *J. Appl. Phys.* **126** 205103
[29] Gundrum B C, Cahill D G and Averback R S 2005 Thermal conductance of metal–metal interfaces *Phys. Rev.* B **72** 245426
[30] Lin Z, Zhigilei L V and Celli V 2008 Electron–phonon coupling and electron heat capacity of metals under conditions of strong electron–phonon nonequilibrium *Phys. Rev.* B **77** 075133
[31] Shahzadeh M, Rahman M, Hellwig O and Pisana S 2018 High-frequency measurements of thermophysical properties of thin films using a modified broad-band frequency domain thermoreflectance approach *Rev. Sci. Instrum.* **89** 084905
[32] Hopkins P E, Beechem T, Duda J C, Hattar K, Ihlefeld J F, Rodriguez M A and Piekos E S 2011 Influence of anisotropy on thermal boundary conductance at solid interfaces *Phys. Rev.* B **84** 125408
[33] Stevens R J, Smith A N and Norris P M 2005 Measurement of thermal boundary conductance of a series of metal-dielectric interfaces by the transient thermoreflectance technique *J. Heat Transfer* **127** 315

[34] Hopkins P E, Kassebaum J L and Norris P M 2009 Effects of electron scattering at metal-nonmetal interfaces on electron–phonon equilibration in gold films *J. Appl. Phys.* **105** 023710
[35] Cheaito R, Gorham C S, Misra A, Hattar K and Hopkins P E 2015 Thermal conductivity measurements via time-domain thermoreflectance for the characterization of radiation induced damage *J. Mater. Res.* **30** 1403
[36] Cheng Z *et al* 2020 Thermal conductance across harmonic-matched epitaxial Al-sapphire heterointerfaces *Community Phys.* **3** 115
[37] Wu J 2009 When group-III nitrides go infrared: new properties and perspectives *J. Appl. Phys.* **106** 011101
[38] Scharoch P, Parliński K and Kiejna A 2000 *Ab initio* calculations of phonon dispersion relations in aluminium *Acta Phys. Pol.* A **97** 349
[39] Bungaro C, Rapcewicz K and Bernholc J 2000 *Ab initio* phonon dispersions of wurtzite AlN, GaN, and InN *Phys. Rev.* B **61** 6720
[40] Fugate R Q and Swenson C A 1969 Specific heat of α Al_2O_3 from 2 to 25 K *J. Appl. Phys.* **40** 3034
[41] Lynn J W, Smith H G and Nicklow R M 1973 Lattice dynamics of gold *Phys. Rev.* B **8** 3493
[42] Prakash J, Pathak L P and Hemkar M P 1975 Phonon dispersion relations for chromium and tantalum *Aust. J. Phys.* **28** 57
[43] Schober H, Strauch D and Dorner B 1993 Lattice dynamics of Al_2O_3 *Z. Phys.* B **92** 273
[44] Brorson S D, Kazeroonian A, Moodera J S, Face D W, Cheng T K, Ippen E P, Dresselhaus M S and Dresselhaus G 1990 Femtosecond room-temperature measurement of the electron–phonon coupling constant in metallic superconductors *Phys. Rev. Lett.* **64** 2172
[45] Jones G H S and Hallett A C H 1960 The specific heat of crystalline SiO_2 between 2 °K and 4 °K *Can. J. Phys.* **38** 696
[46] Mishin Y, Farkas D, Mehl M J and Papaconstantopoulos D A 1999 Interatomic potentials for Al and Ni from experimental data and *ab initio* calculations *Materials Research Society Symp. Proc.* vol **59** p 3393
[47] Chaplot S L, Choudhury N, Ghose S, Rao M N, Mittal R and Goel P 2002 Inelastic neutron scattering and lattice dynamics of minerals *Eur. J. Mineral.* **14** 291
[48] Ho C Y, Powell R W and Liley P E 1972 Thermal conductivity of the elements *J. Phys. Chem. Ref. Data* **1** 279
[49] Kittel C 2005 *Introduction to Solid State Physics* 8th edn (New York: Wiley)
[50] Wei S and Chou M Y 1994 Phonon dispersions of silicon and germanium from first-principles calculations *Phys. Rev.* B **50** 2221
[51] Takeda Y, Lu J and Kishimoto N 2002 Nonlinear response of metal nanoparticle embedded in insulators by 60-keV negative ion implantation *Proc. SPIE* **4934** 46–51